Grain assemblages and diagenesis in organic-rich

Extended

mudrocks, Upper Pennsylvanian Cline shale (Wolfcamp D), Midland Basin, Texas

June 2020 | Junwen Peng , Kitty L. Milliken , Qilong Fu , Xavier Janson , H. Scott Hamlin

ABSTRACT

Grain assemblages in the organic-rich Cline shale in the Midland Basin are dominated by components of extrabasinal derivation (11.4 to 98.5 vol. %; average volume: 82.6%). Major extrabasinal components include K-rich clay minerals, detrital quartz, albite, K-feldspar, micas, and lithic fragments. Intrabasinal components include mainly biosiliceous allochems (sponge spicules and radiolarians), agglutinated foraminifera, Ca-phosphate peloids, clay-rich peloids, organomineralic aggregates, intraclasts, and other biocalcareous allochems. Authigenic minerals are most evident as grain replacements, euhedral ankerite, Ca-phosphate cement, and precipitates in large pores. A strongly localized spatial distribution of diagenetic products at micron to centimeter scales is observed in most siliciclastic samples, except in biosiliceous allochem-rich ones in which abundant intergranular pore-filling clay-size microquartz cement is observed. Compaction is evident in the Cline shale because of low porosity and generally low cement volumes. Neither textural variation nor bulk mineral composition alone is sufficient to confidently decipher the rock bulk property (e.g., total organic carbon) and reservoir quality variation (e.g., porosity and permeability). However, a good negative relationship between the ratio of extrabasinal to intrabasinal grains and favorable reservoir properties is observed in the Cline shale. Specifically, higher porosity, permeability, and total organic carbon are observed in samples representing the extreme end members of intrabasinal-derived biosilica-rich layers. Nickel, a recognized proxy for paleoproductivity, exhibits a positive relationship with intrabasinal grain content and reservoir properties. X-ray fluorescence–based analysis of nickel can be a rapid and cost-effective way to delineate favorable unconventional reservoir quality in the Cline shale.

INTRODUCTION

Despite the status of fine-grained sedimentary rocks (shales, mudstones, and mudrocks) as being the most abundant sedimentary rock type (Folk, 1980) and having global economic significance (Jarvie et al., 2007;

Jarvie, 2012; Zou et al., 2013; Hackley and Cardott, 2016), uncertainties remain concerning the manner in which their basic components affect bulk properties (e.g., total organic carbon [*TOC*]) and reservoir quality (e.g., porosity and permeability).

Heterogeneity of mineral composition, grain assemblages, textural variation, and reservoir quality in organic-rich mudrocks have been well documented in previous studies (e.g., MacQuaker and Gawthorpe, 1993; Macquaker and Howell, 1999; Macquaker and Adams, 2003; Loucks and Ruppel, 2007; Macquaker et al., 2010; Aplin and Macquaker, 2011; Bohacs et al., 2014; K. Milliken, 2014; Lazar et al., 2015; Fairbanks et al., 2016). However, previous work focused mainly on the qualitative description of heterogeneities at multiple scales (from thin section to outcrop). The particular impact of the type of grain assemblage on diagenetic pathways and reservoir quality evolution in mudrocks remains somewhat uncertain and, as a result, is little applied in unconventional reservoir exploration and development. One reason for this uncertainty is the extremely small size of the component grains in mudrocks, which makes direct observation difficult (Folk, 1980). K. Milliken (2014) suggested that most particles in mudrocks are smaller than 30 µm, which is a standard thickness for thin sections. In such fine-grained sedimentary rocks, the identification of grain assemblages and diagenetic features is difficult when using conventional optical microscopy and inadequately captured by scanning electron microscopy (K. Milliken, 2014). Another reason for uncertainty is that the compositional variation in grain assemblages in mudrocks is complex and can include both intrabasinal and extrabasinal particles (e.g., K. Milliken, 2014). Specifically, intrabasinal components include biocalcareous allochems (Denne et al., 2014), biosiliceous allochems (Ellis, 1963; Isaacs, 1981; Young and Moore, 1994; Fishman et al., 2015), organic allochems (water-column dwellers; Passey et al., 2010), and organomineralic aggregates (OMAs) (Macquaker et al., 2010), whereas extrabasinal components mainly include detrital quartz, feldspar, lithic fragments, heavy minerals, terrigenous organic matter (OM), and detrital clay minerals. Such grain-assemblage variations plausibly cause diverse pathways of diagenesis and thus result in different reservoir properties (e.g., porosity, permeability, and mechanical moduli; K. Milliken, 2014).

The Upper Pennsylvanian Cline shale in the Midland Basin, Texas, has long been recognized as an important source rock for productive reservoirs in the basin (Klemme and Ulmishek, 1991). Heightened industry focus on the Cline shale is a result of newly discovered producible unconventional petroleum resources in this marine shale system (Hamlin and Baumgardner, 2012). However, little documentation of

primary grain assemblages, diagenetic features, and rock properties of the Cline shale has been published. Previous studies (K. Milliken, 2014; K. L. Milliken et al., 2017, 2018) indicated that primary grain assemblages (i.e., intrabasinal and extrabasinal grains) with different mechanical and chemical properties are a key factor controlling diagenetic pathway and thus determined bulk reservoir properties, such as porosity, permeability, *TOC*, and mechanical moduli, in several hydrocarbon-producing shale reservoirs (e.g., Barnett, Eagle Ford, and Yanchang). Theoretically, this conclusion from other hydrocarbon-producing shale systems can be also applied to the Cline shale, which has a similar depositional background. Here, we report a case study of how the primary grain assemblages affect diagenetic pathways and rock property (porosity, permeability, and *TOC*) evolution in the Cline shale of the Midland Basin with the goal of elucidating general principles that can inform models for hydrocarbon exploration in fine-grained sedimentary systems.

GEOLOGICAL BACKGROUND

The Cline shale (Wolfcamp D) was deposited in the Midland Basin, an epicratonic foreland basin of the Ouachita orogenic belt and the eastern secondary subsidence tectonic unit of the greater Permian Basin (Figure 1; Yang and Dorobek, 1995). During the Late Pennsylvanian, a time of accelerated subsidence of the Midland Basin, deposition of the Cline shale occurred in the basin, and the Cisco and Canyon Groups of mixed siliciclastic–carbonate composition took place on the Eastern shelf and adjacent area (Wright, 2011; Baumgardner et al., 2016). Since 2009, the Cline shale has been drilled as an unconventional oil reservoir and has been considered as a secondary target in developing the Midland Basin unconventional resource plays (Roush, 2015). For operational purposes, the petroleum industry has long referred to the Cline shale as the Wolfcamp D interval.

The Cline shale of the Midland Basin is underlain by Strawn carbonates and overlain by Wolfcamp strata (Figure 2) and has a thickness ranging from 200 to 425 ft (60 to 130 m) (Roush, 2015). Published structure maps indicate that the Cline shale dips westward (Baumgardner et al., 2016). The Cline shale is bounded by the Eastern shelf to the east, the Central Basin platform to the west, the Ozona arch to the southwest, and the Horseshoe atoll to the north (Figure 1). These four distinct boundaries make the Cline shale a relatively restricted depositional unit.

During sea-level highstand, sediment input to the basin comprised dominantly a combination of platform-

derived wackestone, pelagic calcareous mudrocks, and fine-grained siliciclastics, primarily comprising windblown clay (Brown et al., 1990). By contrast, during sea-level lowstand, platforms were exposed, and siliciclastic sediment-transport systems extended across the wide platform and input directly into the basin (Brown et al., 1990). The Wichita Mountains and the Arbuckle–Criner Hill uplift to the north of the basin provided terrigenous clastics to the basin and the Ouachita orogenic belt to the east of the Eastern shelf is another important clastic source area (Brown et al., 1990).

Global plate reconstructions by Blakey (2003) suggested that during the Late Pennsylvanian, the Midland Basin occupied a narrow inland seaway (Great Permian seaway) bounded by the Laurussian continent to the north and Gondwana to the south. Water circulation in the Midland Basin was restricted by stratification (development of both a thermocline and chemocline), forming the bottom anoxic environment (Algeo and Heckel, 2008). Water depths across the southern Midland Basin are difficult to estimate. Algeo and Heckel (2008) suggested that bathymetric variation in the Permian Basin region during the Late Pennsylvanian was considerable, with deep basins (hundreds of meters) separated by shallower sills that formed over structural highs. This range of water depth is similar to the early Permian Wolfcamp basinal setting in the Midland Basin, which is estimated to be 1000–2000 ft (300–600 m; Baumgardner et al., 2016).

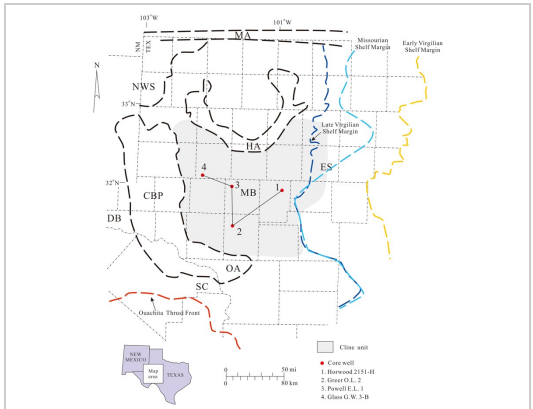

Figure 1. Map of the Midland Basin showing the distribution of the Cline shale, general structural features, location of cores, and regional cross section. Map modified from Wright (2011) and Baumgardner et al. (2016). Bold, dotted black lines are the boundary of tectonic unit. CBP = Central Basin platform; DB = Delaware Basin; ES = Eastern shelf; HA = Horseshoe atoll; MA = Matador arch; MB = Midland Basin; NM = New Mexico; NWS = Northwest shelf; OA = Ozona arch; SC = Sheffield channel; TEX = Texas.

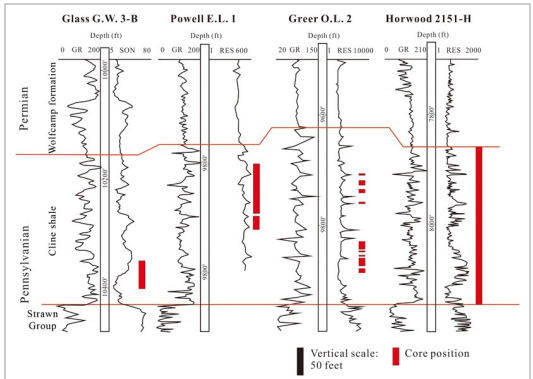

Figure 2. General stratigraphy of the Upper Pennsylvanian to lower Permian section in the Midland Basin. Location of the section was shown in Figure 1. Top of Strawn Formation carbonate is used as datum. Horizontal red lines represent formation boundary. Jagged black lines represent well logs. GR = gamma ray in API units; RES =

SAMPLING AND ANALYTICAL METHODS

The four cores from the southern Midland Basin used in this

resistivity in ohm-meters; SON = sonic in microseconds per feet.

study are located in Sterling, Reagan, Glasscock, and Martin Counties (Figure 1). The core from the Horwood 2151-H well is continuous (273 ft [83 m] in total) and penetrates through the whole Cline shale (Figure 2). The Greer O. L. 2, Glass G. W. 3-B, and Powell E. L. 1 wells are cored only in several short intervals (Figure 2). All of these cores are stored at the Core Research Center, Bureau of Economic Geology, The University of Texas at Austin.

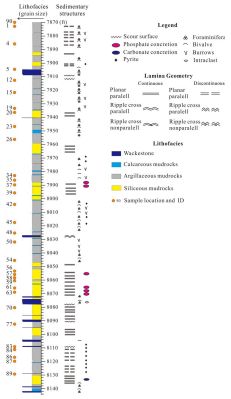

Figure 3. Simplified core description of Horwood 2151-H with sample locations. Mudrock terminology used here is modified from Lazar et al. (2015). Left-point arrows indicate the direction of increasing grain size. ID = identification number.

In total, 140 samples were taken from four wells to prepare polished thin sections. Among these 140 samples, 35 were chosen for systematic bulk mineralogy x-ray diffraction (XRD) analysis, *TOC* analysis, field-emission scanning electron microscopy observation, whole-rock elemental analysis by x-ray fluorescence (XRF), and porosity and permeability measurement (using the Gas Research Institute [GRI] method; Guidry et al., 1996). For these 35 chosen samples, the Horwood 2151-H well was sampled in detail (32 samples) to assess mudrock heterogeneity in grain assemblages, petrophysical properties, and geochemical properties (Figure 3); the other 3 samples are from the remaining three wells (Table 1). The following were used as sampling criteria: (1) volumetrically significant major and minor lithologies and (2) material that is as homogeneous as possible within the individual sampling intervals (<2 in.) so that the different types of analyses made on subsamples can be correlated.

Bulk Composition Analysis

Element analyses were undertaken using Bruker Elemental Tracer IV-SD energy-dispersive XRF equipment. The XRF spectra for major elements were generated under vacuum using a rhodium (Rh) tube set at 15 kilovolts (kV) and 34.4 microampules (μA) for a count time of 60 s. The XRF spectra for trace elements were analyzed at 40 kV and 25 μA, with an Al-Ti-copper (Cu) filter on the equipment and a count time of 60 s. Core samples were analyzed by placing the flat slab side down on the nose of the instrument. Calibration

during and after measurement rigorously followed the workflow proposed by Rowe et al. (2012).

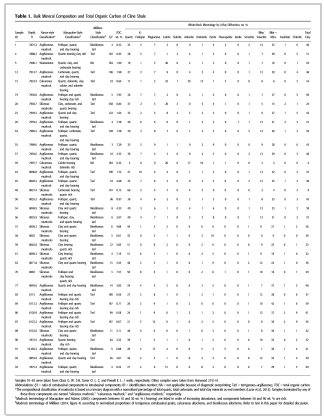

The XRD, *TOC*, and GRI's crushed-rock porosity and permeability measurement were completed by FireWheel Energy LLC (Houston, Texas). X-ray patterns of the sample powders (~500 mg) are recorded on a Bruker D8 Advance powder x-ray Diffractometer using Cu radiation (40 kV and 100 milliampules) from a long line focus tube, a graphite monochromator in the diffracted beam, and a vacuum device to minimize absorption of the x-rays by air. Identification of minerals is made using EVA software (Bruker AXS Inc.) by comparison to reference mineral patterns archived in the Powder Diffraction Files of the International Centre for Diffraction Data. The XRD results are given as weight percentage. These analytical data were previously reported in the appendix of Zheng (2016).

Imaging Technology

Uncovered polished thin sections of approximately 25 µm thickness were produced for optical microscopy and scanning electron microscope (SEM) imaging. Samples were first inspected using conventional petrographic microscopy and were then coated with approximately 25 nanometers carbon (C) before being examined in the Field Electron and Ion Nova NanoSEM 430 field emission-SEM. All 35 samples were examined using both secondary electron (SE) and backscattered electron (BSE) modes. Elemental and mineral composition was identified by x-ray energy-dispersive spectroscopy (EDS) mapping. A unified scheme of false color was applied to the major mudrock elements to discriminate minerals: potassium (K) (yellow; K-feldspar, muscovite, and K-clay); silicon (red; quartz); sodium (Na) (aqua; Na-feldspar); magnesium (Mg) (fuchsia; dolomite, chlorite); calcium (Ca) (blue; calcite); iron (yellow; pyrite); and C (orange; OM). Twin 30-mm^2 Bruker XFlash silicon drift detector EDS detectors were equipped using 15 kV accelerating voltage, 5.0 µm spot size, 30 µm aperture, a working distance of approximately 9–10 mm, and more than 500 s scanning time. Cathodoluminescence (CL) imaging using a Gatan ChromaCL detector was conducted on some specific samples to distinguish authigenic quartz and detrital quartz. The CL imaging was performed using 15 kV accelerating voltage, 5.0 µm spot size, 40 µm aperture, a working distance of approximately 12–13 mm, and 10 min of scanning time. The EDS maps were mixed with BSE maps, and the

CL maps were mixed with the SE signal to create the images presented in this study.

Point-Count and Grain-Tracing Methods

A grain-assemblage point count was conducted on EDS maps using the image analysis program JMicrovision© (Roduit, 2008). The EDS mapping was performed at magnifications of 2500× to 3000× for all samples in this study. This is because we can confidently identify detrital silt particles at these magnifications. Areas having anomalously large allochems (commonly extra large, robust molluscan skeletal and agglutinated foraminifera) were intentionally avoided. Two images were taken of each sample to obtain a 200 × 200 μm^2 area, which we believe approaches the representative elementary area suggested for mudrocks in previous studies (Yoon and Dewers, 2013; Houben et al., 2014; Kelly et al., 2016). For each image, 200 random points were counted (a total of 400 points for each sample).

Particle-size determination for the silt fraction (grain size between 4 and 9 ϕ or 63 and 2 μm) was performed on BSE images within the area of point counting. A boundary of 2 μm is used in this study to distinguish silt-size particles and clay-size particles. This is because we can confidently identify detrital particles of 2-μm diameter under SEM magnifications of 2500× to 3000×. Grain outlines were manually traced using the image analysis program JMicrovision (Roduit, 2008). Grain size is expressed as equivalent circular diameter (ECD), which by definition is the diameter of a circle having the same area as that of the object. All grains greater than 2 μm (>0.00008 in.) or 9 ϕ, except authigenic crystals, which were fully within the field of view, were included in the measurement. Mean grain size data from these all-grain images were corrected to standard volume-weighted mean grain size based on the grain area fraction (individual grain areas are normalized to total grain area, a proxy for volume).

RESULTS

Bulk Composition and Lithology

Bulk composition analysis data in this study, including XRF, XRD, *TOC*, porosity, and permeability, are given in Table 1 and the Appendix (supplementary material available as AAPG Datashare 120 at www.aapg.org/datashare). Clay minerals are the most important component in the Cline shale, ranging from 4 to 61 wt. % (mean of 40 wt. %; Table 1). Excluding kaolinite (authigenic pore filling) and chlorite

(also dominantly authigenic), the average content of probable detrital clay (reported as smectite, illite, and mixed-layer illite–smectite in Table 1) is approximately 36 wt. %, ranging from 4 to 53 wt. %. Pore-filling crystalline illite can also be identified locally. Quartz is another important mineral in the Cline shale, ranging from 3 to 66 wt. % (mean of 34 wt. %). Carbonate minerals, including calcite, dolomite, ankerite, and siderite, are abundant in only three samples (i.e., samples 15, 39, and 54) of the wackestone and calcareous mudrock facies (Table 1). Excluding these three carbonate samples, calcite is detected in all but four of the samples, averaging approximately 3 wt. % and ranging from below detection to 20 wt. %, whereas dolomite and ankerite range from below detection to 8 wt. % (mean of 2 wt. %) and below detection to 4 wt. % (mean of 1 wt. %), respectively. Feldspars, including plagioclase and K-feldspar, are also important components, averaging 9 wt. % and ranging from below detection to 17 wt. %. Pyrite ranges from below detection to 10 wt. % (mean of 4 wt. %). Other minor minerals detected by XRD include siderite, barite, and apatite (Table 1).

The lithofacies nomenclature of mudrocks used in this study is modified from the compositional classification proposed by Lazar et al. (2015). Mudrocks dominated by quartz; carbonate (e.g., calcite, dolomite, etc.); or clay minerals (e.g., illite, smectite, etc.) are named "siliceous mudrock," "calcareous mudrock," and "argillaceous mudrock," respectively. Based on the XRD analysis of 15 mineral compositions (Table 1) and petrographic observations (described below), 4 lithologies were recognized: siliceous mudrocks, calcareous mudrocks, argillaceous mudrocks, and wackestone (Figure 3; Table 1). The *TOC* varies significantly, even for the same lithofacies over short vertical distances. Measured *TOC* ranges from 0.13 to 8.32 wt. % with a mean value of 3.48 wt. % (Table 1).

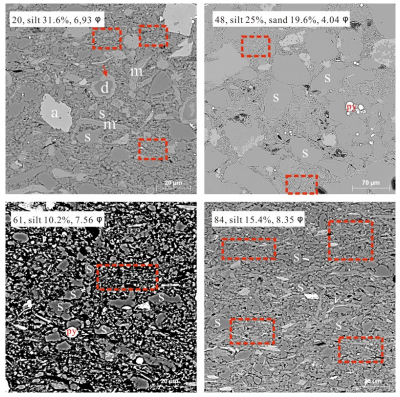

Figure 4. Textural variations observed in backscattered electron images. Images for samples 20, 48, 61, and 84 illustrate variations in silt and sand content. Data obtained from JMicrovision (Roduit, 2008). The four samples selected represent important textural variations: sample 84 contains the finest mean silt size (8.35 ϕ); sample 61 contains the least silt (10.2%) but has a coarser mean grain size than sample 84; sample 48 contains abundant silt and also sand-size particles; sample 20 contains the highest silt content (31.6%). Examples of silt- and sand-size particles are labeled "s" in each image. Detrital

Textural Variation

All of the samples examined in this study are composed of clay- and silt-size grains, except sample 48, which also

dolomite (labeled “d”) with ankerite rim (red arrow), ankerite (labeled “a”), pyrite (labeled “py”), and silt-size micas (labeled “m”) are also observed in some samples. The red dashed line boxes highlight regions rich in clay-size matrix.

contains a substantial amount of sand-size particles (19.6 vol. %). Silt plus sand content ranges from 10.2 to 44.6 vol. % (Table 2). The corrected mean ECD of silt and sand grains ranges from 4.04 to 8.35 ϕ. The ϕ standard deviation ranges from 0.39 to 1.07, which suggests a wide range of grain sorting. Some examples of end-member textures of the silt- and sand-size particle distribution pattern are shown in Figures 4 and 5. Based on the textural classification of Macquaker and Adams (2003), all of the samples belong to silt-bearing clay-rich mudstone, except sample 48, which is sand- and silt-bearing clay-rich mudstone (Table 2).

Table 2. Grain-Tracing Textural Variation of Cline Shale

		Textural Variation			
Sample ID	Textural Lithology*	Median, φ	Mean, φ	Sorting, φ	Silt Content, vol. %
1	Silt-bearing clay rich	8.45	7.52	0.52	12.00%
4	Silt-bearing clay rich	8.06	7.13	0.6	19.80%
5	NA				
12	Silt-bearing clay rich	8.32	7.13	0.57	20.40%
15	NA				
19	Silt-bearing clay rich	8.34	7.5	0.55	11.90%
20	Silt-bearing clay rich	8.21	6.93	0.67	31.60%
26	Silt-bearing clay rich	8.4	7.65	0.5	15.70%
54	Silt-bearing clay rich	8.05	7.12	0.61	29.20%
55	Silt-bearing clay rich	8.41	7.7	0.52	13.20%
57	Silt-bearing clay rich	8.14	6.99	0.53	20.00%
39	NA				
45	Silt-bearing clay rich	8.06	7.07	0.61	21.70%
48	Sand and silt-bearing clay rich	6.54	4.04	1.07	25% (19.6%)†
50	Silt-bearing clay rich	7.88	6.73	0.69	26.60%
54	Silt-bearing clay rich	8.2	7.46	0.51	14.40%
56	Silt-bearing clay rich	7.97	7.04	0.59	17.00%
59	Silt-bearing clay rich	8.29	7.81	0.44	13.40%
61	Silt-bearing clay rich	8.25	7.56	0.49	10.20%
63	Silt-bearing clay rich	8.36	7.72	0.47	15.40%
70	Silt-bearing clay rich	8.32	7.6	0.5	12.80%
85	Silt-bearing clay rich	8.19	7.52	0.48	12.00%
89	Silt-bearing clay rich	8.48	7.8	0.48	12.60%
90	Silt-bearing clay rich	7.78	6.78	0.63	29.70%
91	Silt-bearing clay rich	8.11	6.95	0.69	14.90%
92	Silt-bearing clay rich	8.37	7.14	0.89	17.30%
93	Silt-bearing clay rich	7.81	6.69	0.76	28.40%
23	Silt-bearing clay rich	8.06	6.84	0.66	19.19%
84	Silt-bearing clay rich	8.38	8.35	0.49	13.44%
86	Silt-bearing clay rich	8.44	8.09	0.39	12.23%
87	Silt-bearing clay rich	8.44	8.11	0.39	13.28%
42	Silt-bearing clay rich	8.43	7.55	0.53	12.94%
77	Silt-bearing clay rich	8.02	6.88	0.64	20.18%
57	Silt-bearing clay rich	8.17	6.47	0.62	18.55%
58	Silt-bearing clay rich	8.44	7.42	0.55	14.55%

Abbreviations: ID = identification number; NA = not applicable because of diagenetic overprinting.
*Following Macquaker and Adams (2003), based on volume percent.
†Only sample 48 contained a sand-size fraction. The number in parentheses in sample 48 is the sand-size fraction (grain size >4 φ). The number outside the parentheses in sample 48 includes both the silt- and sand-size fractions.

Major Extrabasinal Grains

In general, extrabasinal particles include detrital quartz, feldspar, lithic fragments, mica, and terrigenous OM (Figures 6). Detrital silt-size quartz is very common in most of the Cline shale. Detrital quartz is characterized by its angular shape (Figures 6). Figures 7 shows the most common reddish CL color of silt-size detrital quartz. Some specific silt-size detrital quartz can exhibit CL color from dark red to bright blue (Figure 7C, D). Some fabrics, such as microfractures and overgrowth zones of detrital quartz, can also be identified by CL (Figure 7C, D).

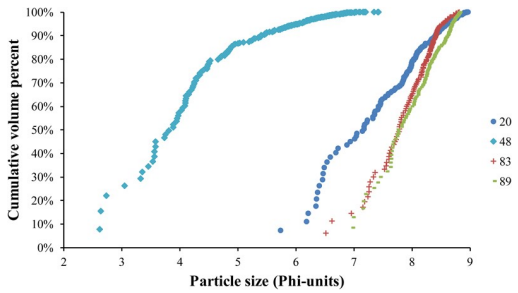

Figure 5. Variations in the particle-size distribution of the four samples in Figure 4.

Detrital silt-size feldspar includes K-feldspar and albite (Figures 6). The most common lithic grains are quartz-feldspar aggregates, which may correspond to plutonic rock fragments (Folk, 1980; K. L. Milliken et al., 2017) (Figures 6). Monocrystalline micas include K-rich mica (muscovite) and Mg-rich mica (chlorite) (Figures 6).

A component of terrigenous OM (woody material characterized by particle shapes that reflect the cell structure typical of woody material) is present in the silt- and sand-size fraction (Figure 8A), but the volume of this material is relatively minor compared to other OM types (refer to next section).

The dominant clay mineral is K rich (Figures 6). Bulk XRD analysis data indicate that this clay may most likely be a mixed layer of illite–smectite and illite.

Three carbonate samples (i.e., samples 5, 15, and 39) have experienced heavy diagenesis overprinting; thus, the original grain assemblage cannot be identified with precision. As a result, little information of grain assemblage can be obtained from them. Except for carbonate samples, extrabasinal grains account for approximately 87.5 vol. % of total grains, ranging from 69.5 to 98.5 vol. % on the basis of point count (Appendix, supplementary material available as AAPG Datashare 120 at www.aapg.org/datashare).

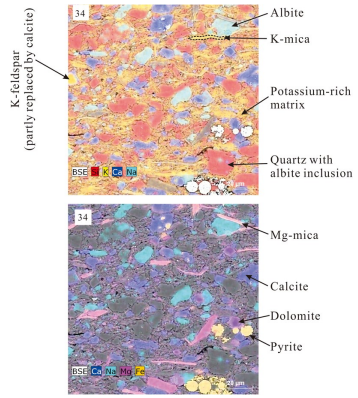

Figure 6. Major extrabasinal components observed in x-ray energy-dispersive spectroscopy mapping, sample 34. Silt-size detrital quartz, K-mica, Mg-mica, albite, and K-feldspar are abundant in rocks. The dominant clay mineral is K rich. Bulk x-ray diffraction analysis data indicate that this clay may most likely be a mixed layer of illite–smectite and illite. BSE = backscattered electron.

Major Intrabasinal Grains

Criteria for identification of intrabasinal grains follow Scholle and Ulmer-Scholle (2003). Intrabasinal grains are identified based on their size, shape, internal structure, mineral composition, and age range. Major intrabasinal particles observed under the SEM include biosiliceous allochems (sponge spicules and radiolarians; Figure 9A, B); agglutinated foraminifera (Figure 9C), biocalcareous allochems (Figure 9D); OMAs (Figure 9E); Ca-phosphate peloids (Figure 9F); and intraclasts (phosphatic grains, vertebrate bones and teeth, and glauconite; Figure 10).

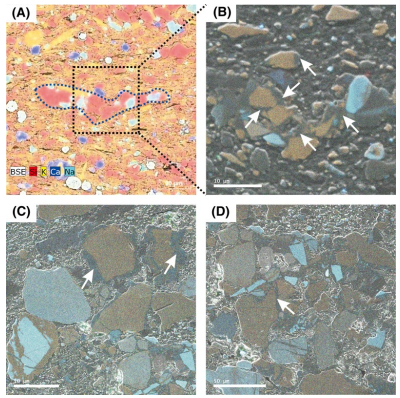

Figure 7. Representative extrabasinal detrital quartz in the Cline shale. (A) X-ray energy-dispersive spectroscopy map of agglutinated foraminifera (dark-blue dashed line); sample 37. (B) Cathodoluminescence image of a close-up area in (A). Detrital quartz exhibits a reddish color. White arrows indicate quartz cement. (C) Cathodoluminescence image of detrital quartz shows cathodoluminescence color range from dark

red to bright blue. White arrows indicate quartz cement; sample 48. (D) Cathodoluminescence image of detrital quartz shows cathodoluminescence color range from dark red to bright blue. The white arrow indicates quartz cement (dark-blue color); sample 83. BSE = backscattered electron.

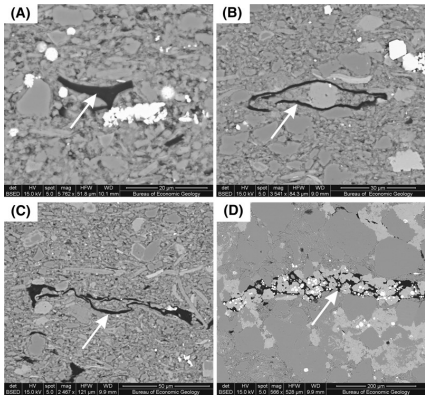

Figure 8. Organic matter types identified in the Cline shale. (A) Organic matter particle of likely terrigenous origin (white arrow), sample 63. (B) Possible algal spore (white arrow); sample 43. (C) Possible algal spore (white arrow) partially collapsed by compaction, sample 12. (D) Migrated bitumen (white arrow), sample 47. det = detector; det BSED = backscattered electron detector; HFW = horizontal field width; HV = accelerating voltage; mag = magnification; spot = spot size; WD = working distance.

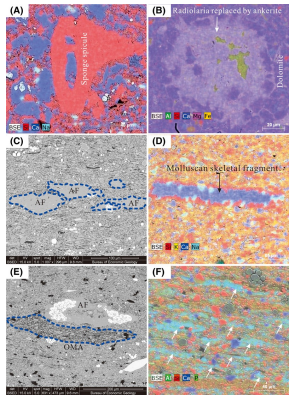

Figure 9. Representative intrabasinal grains in the Cline shale. (A) X-ray energy-dispersive spectroscopy map showing sponge spicule, sample 59; (B) x-ray energy-dispersive spectroscopy map showing radiolaria (replaced by ankerite) and pore-filling kaolinite, sample 39; (C) agglutinated foraminifera (AF) (dashed blue line), backscattered electron (BSE) image, sample 2; (D) x-ray energy-dispersive spectroscopy map showing molluscan skeletal fragment, sample 34; (E) AF (partly replaced by pyrite) and organomineralic aggregates (OMAs) (dashed blue line), BSE image, sample 1; and (F) x-ray energy-dispersive spectroscopy map showing plausible Ca-phosphate peloids (arrows), sample 35. det = detector; det BSED = backcattered electron detector; HFW = horizontal field width; HV = accelerating voltage; mag = magnification; spot = spot size; WD = working distance.

Please log in to read the full article

Log in to Submit a Comment

Comments (0)

You may also be interested in ...

Popular articles